AIP | Review of Scientific Instruments

A magnetic particle time-of-flight (MagPTOF) diagnostic for measurements of shock- and compression-bang time at the NIF (invited)a)

H. G. Rinderknecht, H. Sio, J. A. Frenje, J. Magoon, A. Agliata, M. Shoup, S. Ayers, C. G. Bailey, M. Gatu Johnson, A. B. Zylstra, N. Sinenian, M. J. Rosenberg, C. K. Li, F. H. Sèguin, R. D. Petrasso, J. R. Rygg, J. R. Kimbrough, A. Mackinnon, P. Bell, R. Bionta, T. Clancy, R. Zacharias, A. House, T. Döppner, H. S. Park, S. LePape, O. Landen, N. Meezan, H. Robey, V. U. Glebov, M. Hohenberger, C. Stoeckl, T. C. Sangster, C. Li, J. Parat, R. Olson, J. Kline, and J. Kilkenny

Citation: Review of Scientific Instruments **85**, 11D901 (2014); doi: 10.1063/1.4886775
View online: http://dx.doi.org/10.1063/1.4886775
View Table of Contents: http://scitation.aip.org/content/aip/journal/rsi/85/11?ver=pdfcov
Published by the AIP Publishing

A magnetic particle time-of-flight (MagPTOF) diagnostic for measurements of shock- and compression-bang time at the NIF (invited)[a)]

H. G. Rinderknecht,[1,b)] H. Sio,[1] J. A. Frenje,[1] J. Magoon,[2] A. Agliata,[2] M. Shoup,[2] S. Ayers,[3] C. G. Bailey,[3] M. Gatu Johnson,[1] A. B. Zylstra,[1] N. Sinenian,[1] M. J. Rosenberg,[1] C. K. Li,[1] F. H. Sèguin,[1] R. D. Petrasso,[1] J. R. Rygg,[3] J. R. Kimbrough,[3] A. Mackinnon,[3] P. Bell,[3] R. Bionta,[3] T. Clancy,[3] R. Zacharias,[3] A. House,[3] T. Döppner,[3] H. S. Park,[3] S. LePape,[3] O. Landen,[3] N. Meezan,[3] H. Robey,[3] V. U. Glebov,[2] M. Hohenberger,[2] C. Stoeckl,[2] T. C. Sangster,[2] C. Li,[4] J. Parat,[4] R. Olson,[5] J. Kline,[6] and J. Kilkenny[7]
[1]*Massachusetts Institute of Technology, Cambridge, Massachusetts 02139, USA*
[2]*Laboratory for Laser Energetics, Rochester, New York 14623, USA*
[3]*Lawrence Livermore National Laboratory, Livermore, California 94550, USA*
[4]*Dexter Magnetic Technologies, Elk Grove Village, Illinois 60007, USA*
[5]*Sandia National Laboratory, Albuquerque, New Mexico 87123, USA*
[6]*Los Alamos National Laboratory, Los Alamos, New Mexico 87545, USA*
[7]*General Atomics, San Diego, California 92121, USA*

(Presented 3 June 2014; received 1 June 2014; accepted 22 June 2014; published online 14 July 2014)

A magnetic particle time-of-flight (MagPTOF) diagnostic has been designed to measure shock- and compression-bang time using D^3He-fusion protons and DD-fusion neutrons, respectively, at the National Ignition Facility (NIF). This capability, in combination with shock-burn weighted areal density measurements, will significantly constrain the modeling of the implosion dynamics. This design is an upgrade to the existing particle time-of-flight (pTOF) diagnostic, which records bang times using DD or DT neutrons with an accuracy better than ±70 ps [H. G. Rinderknecht *et al.*, Rev. Sci. Instrum. **83**, 10D902 (2012)]. The inclusion of a deflecting magnet will increase D^3He-proton signal-to-background by a factor of 1000, allowing for the first time simultaneous measurements of shock- and compression-bang times in D^3He-filled surrogate implosions at the NIF. © *2014 AIP Publishing LLC*. [http://dx.doi.org/10.1063/1.4886775]

I. INTRODUCTION

Recent experiments at the National Ignition Facility (NIF)[1] have made substantial progress in the effort towards fusion ignition of an inertially confined implosion. Better understanding and optimization of the 1D performance of implosions at the NIF has been identified as an important path forward to attaining ignition.[2] Shock burn, a brief period of fusion production during the shock collapse and rebound at the center of the implosion, is closely associated with the strength of the shock. The rebounding shock striking the imploding fuel and shell also initiates deceleration, which culminates in peak fuel compression and burn. A direct measurement of the shock-bang time and the time difference between shock- and compression-bang time (ΔBT) will provide valuable new constraints on the 1D physics of the shock propagation and shell deceleration, improving the understanding of the in-flight conditions of the fuel and shell. In hydrodynamic simulations of NIF-scale implosions, ΔBT is insensitive to changes in the experimental parameters. However, experimental evidence seems to suggest that ΔBT may be changing by as much as 50%.[3]

In implosions with deuterium and helium-3 gas fill, the rebounding shock heats the central fuel and initiates $D(^3He,p)^4He$ fusion reactions which produce 14.7 MeV protons. The spectrum of the emitted D^3He protons is measured by the Wedge Range-Filter (WRF) proton spectrometers,[4] and from the energy downshift, the total areal density (fuel and shell ρR) of the implosion is measured.[5] Comparisons of ρR at shock-bang time to time-resolved x-ray radiographs of the implosion trajectory[6,7] indicate that the data are best explained by a change in ΔBT of approximately 400 ps as coasting is varied from 1 to 2.5 ns.[3] Since these shifts are not reproduced in simulations, they suggest that the timing of the shock collapse at the center of the implosion and of the subsequent onset of the deceleration phase are not well understood. A direct measurement of ΔBT would strongly constrain models of shock-propagation and deceleration-phase dynamics.

An upgrade to the particle time-of-flight (pTOF) diagnostic[8] has been designed to provide measurements of both shock- and compression-bang time by time-resolved observation of D^3He-proton and DD-neutron production, respectively. The pTOF has accurately measured bang times at the NIF using DT- and DD-fusion neutrons for over 3 years, and has also measured bang-time in polar-direct-drive implosions using D^3He-protons.[8] In polar-direct-drive implosions using D_2 fuel, pTOF has recorded both primary DD-neutrons and secondary D^3He-protons, with yields comparable to those observed at compression- and shock-burn, respectively, in

[a)]Invited paper, published as part of the Proceedings of the 20th Topical Conference on High-Temperature Plasma Diagnostics, Atlanta, Georgia, USA, June 2014.
[b)]hgr@mit.edu

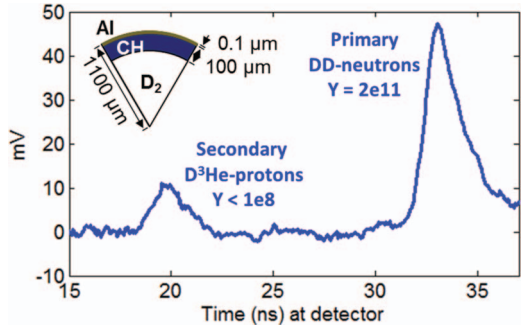

FIG. 1. pTOF signal trace from NIF Polar-Direct-Drive (PDD) implosion N140306-003 with background subtracted, on which pTOF measured both primary DD-neutrons (Yield $= 2 \times 10^{11}$) and secondary D^3He-protons (Yield $< 10^8$). Due to the limited x-ray fluence on PDD implosions, pTOF could be fielded with reduced high-Z filtering, enabling measurement of D^3He-protons. This measurement demonstrates the proof-of-concept for shock- and compression-bang time measurements using the MagPTOF detector, which will have comparable nuclear yields to those recorded here.

indirectly driven D^3He gas-filled implosions. This data, shown in Figure 1, provide a proof-of-principle for measuring ΔBT using these species. However, for indirect-drive implosions, the substantial shielding required to limit x-ray background to acceptable levels prevents the D^3He-protons from being detected. By including a small dipole magnet, the Magnetic pTOF (MagPTOF) will deflect protons around the shielding and onto the detector, allowing for simultaneous measurements of D^3He-protons and DD-neutrons produced at shock-burn and compression-burn, respectively.

Section II of this paper discusses the design of the MagPTOF diagnostic for the NIF. Optimizations to the magnet and calculations of the proton trajectories through the magnet design are presented in Sec. III, and the predicted signal and dominant sources of background are discussed in Sec. IV. The conclusions are presented in Sec. V.

II. DESIGN

The MagPTOF diagnostic represents a significant upgrade to the existing pTOF diagnostic on the NIF, and includes four main components, depicted schematically in Figure 2. The MagPTOF detector, cables, bias, and oscilloscope systems are identical to the existing pTOF system, which is described in detail in Ref. 8. The detector, nominally positioned 49 cm from the implosion, detects protons between 6 and 16 MeV. X-ray shielding made of tungsten cylinders protects the detector from direct x-ray fluence from the hohlraum. This shielding may be configured in units of 0.5 cm up to a maximum of 4 cm, depending on the predicted level of x-ray background. A permanent dipole magnet with a peak field of approximately 1 T deflects protons around the shielding and onto the detector. Lastly, an annular piece of CR-39 nuclear track detector[9] can be positioned around the pTOF detector, to confirm proton fluence and energy on the detector after each experiment.

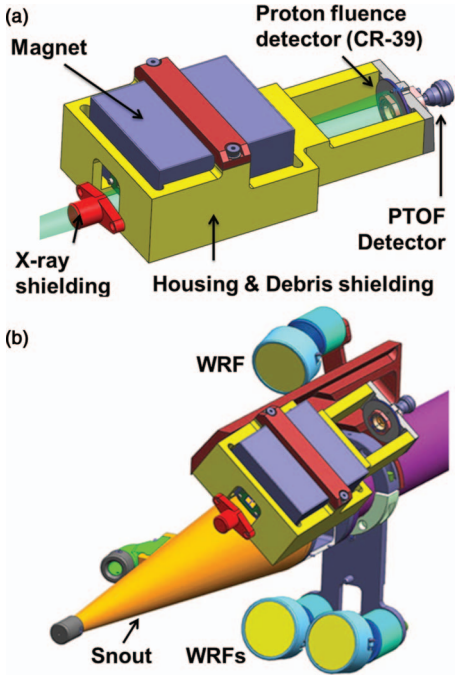

FIG. 3. 3D-models of the MagPTOF engineering design. (a) The x-ray shielding (red cylinder), aperture and magnet (purple), detector (gold), and annular CR-39 (blue) are held in relative alignment by an aluminum housing (yellow). Target chamber center (TCC)-facing components will be sheathed in stainless steel for ablation resistance and debris protection. The point-projection shadow of the shielding from TCC (green transparent) has a radius in the detector plane of $\sim 3\times$ the detector's active radius. (b) The MagPTOF is attached to the NIF DIM (90,78) snout with a stainless-steel mounting arm (red), alongside a WRF spectrometer (blue).

An engineering design for the diagnostic that meets NIF requirements has been completed. The MagPTOF assembly shown in Fig. 3(a) maintains the relative alignment of the magnet, x-ray shielding, and detector. The housing is made of aluminum to reduce weight; surfaces facing target chamber center are covered with stainless steel for ablation resistance and debris shielding. This assembly weighs approximately 4 kg. Like the pTOF diagnostic, the MagPTOF assembly is fielded on the diagnostic instrument manipulator (DIM)[10] installed on the NIF target chamber at the angular position

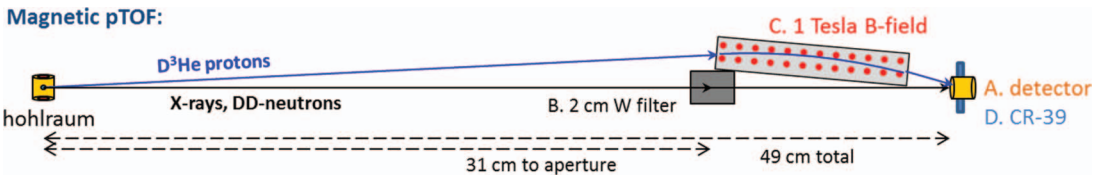

FIG. 2. A schematic of the MagPTOF diagnostic on the NIF. The diagnostic includes four main components: (A) CVD-diamond detector, (B) x-ray shielding (tungsten, configurable in units of 0.5 cm up to 4 cm) to shield the detector from hohlraum x-ray background, (C) a permanent dipole magnet with 1 T peak field to deflect protons around the shielding and onto the detector, and (D) optional annular piece of CR-39 around the CVD-diamond, to confirm proton fluence and energy on each shot. The MagPTOF detector, cables, and electronics are identical to the existing ones for the pTOF.

($\theta = 90°$, $\phi = 78°$), as shown in Fig. 3(b). The MagPTOF mounting bracket replaces the upper half of the previous 4-position pTOF/WRF mounting bracket with an alternate design to support the added weight of the MagPTOF assembly. The center of the magnet aperture is positioned 13.6° above the equator, matching the polar angle of the neighboring WRF. For cylindrically symmetric hohlraum designs, the protons incident on both MagPTOF and WRF will be ranged through identical hohlraum profiles, and proton spectra will be identical along both lines of sight. Since the evaluation of shock bang-time from the MagPTOF proton data requires precise knowledge of the proton energy, matching the WRF polar line-of-sight reduces the uncertainty in the measurement. The location of the adjacent upper WRF in the target chamber is maintained from the previous 4-position design. The hardware holding the two WRFs below the equator is unchanged.

III. MAGNET OPTIMIZATION

D^3He-protons emitted from NIF hohlraum implosions typically have a peak energy in the range 8-12 MeV, accounting for energy downshift in both the imploding capsule and the hohlraum wall. A magnet has been optimized for the MagPTOF system, to reliably deflect protons in this energy range onto the CVD-diamond detector without requiring active controls or detailed knowledge of the proton spectrum prior to the experiment.

The deflecting magnet, a permanent dipole to be manufactured by Dexter Magnetic Technologies, is composed of $Nd_2Fe_{14}B$, with a density of 7.4 g/cc, and is sheathed in vacuum-tight autenistic stainless steel to prevent outgassing of the glue compound into the NIF target chamber. The magnet has a pole gap of 1.5 cm, a pole depth of 2 cm, and is 8 cm long. The aperture in front of the magnet is positioned 31 cm from the implosion, subtending a solid angle fraction of 1.08×10^{-4}.

A peak field of 1 Tesla deflects incident protons away from the magnet's yoke into the region behind the x-ray shielding. The radius of curvature for a charged particle in a magnetic field is $R_{gyro} = p/qB$, where p is the particle momentum, q its charge and B the magnetic field strength. For a 10 MeV proton traveling through the MagPTOF magnet, the peak radius of curvature will be approximately 50.9 cm. This proton's path will be deflected by approximately 9° after transiting the magnet. To maximize the path length of the protons in the magnetic field, the body of the magnet is rotated 4° in the bending plane. This rotation balances the entrance and exit angles for 10 MeV protons arriving at the magnet from TCC, and also introduces a weak focusing of protons in the bending plane.

A series of proton trajectory calculations were performed using the geometry and modeled field of the magnet described in Sec. II. In the nominal geometry, the detector records protons generated at TCC with energy in the range 6 to 16 MeV, as shown in Figure 4. The effective solid angle fraction of the detector is above the nominal detector solid angle fraction of 1.7×10^{-5} for protons in the energy range 8 to 16 MeV, and is approximately 1.8×10^{-5} for 10 MeV protons. This ~10% focusing effect arises from a combination of focusing in the cross-field direction and defocusing in the parallel-field direction.

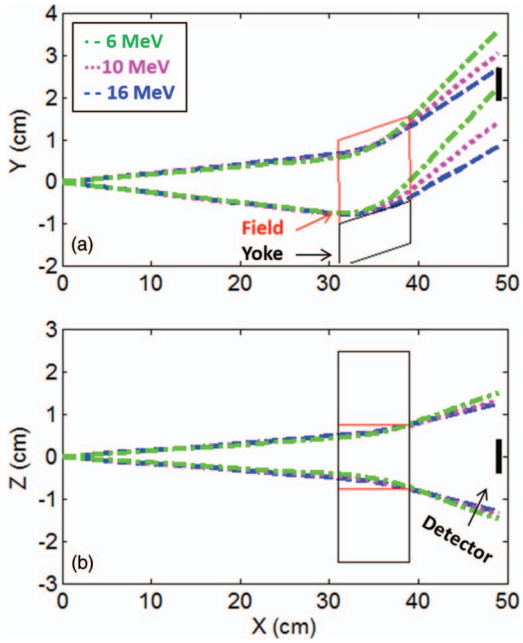

FIG. 4. (a) Calculated proton trajectories for the MagPTOF system projected to the bending plane (x,y). (b) Calculated trajectories projected perpendicular to the bending plane (x,z). Protons with energy 6, 10, and 16 MeV (green dot-dashed, magenta dotted, and blue dashed, respectively) were launched from the origin and transported through the dipole magnetic field (red) to the detector plane (black). Effective solid angle fraction of the detector was found to be above 1.7×10^{-5} for protons in the energy range 8–16 MeV.

An important design consideration for the magnet is to minimize the effect of misalignment on the proton signal level. As the diagnostic is mounted onto the side of x-ray diagnostic snouts fielded on DIM (90,78), the system is not independently pointed and must be designed to function correctly with any DIM instruments. In practice, nominal insertion depth of the existing pTOF diagnostic has varied by ±1 cm, depending on the DIM instrument installed. With the magnet line-of-sight nominally aligned to 13.6° above the equator, this insertion depth variation translates into approximately ±0.4° of misalignment in the bending plane (dispersion direction).

To evaluate the effect of mispointing the MagPTOF, proton trajectory calculations were also made for proton launch points moved by ±1 cm both in the bending-plane and perpendicular to the bending plane, corresponding to a ±1.6° angular mispointing. Figure 5 shows the results of this study, which indicate that the design robustly transport protons to the detector with an effective solid angle fraction of $\sim 1.6 \times 10^{-5}$ or higher for misalignment of ±1.6° in all directions, well beyond the expected alignment uncertainty.

Temporal broadening of the proton signal due to increased path-lengths in the system was also examined, and the results for 10 MeV protons are shown in Figure 6. For all proton energies studied, this magnet design introduced a temporal broadening of less than ±7 ps, well below other timing uncertainties. For comparison, typical proton spectra measured in D^3He gas-filled implosions at the NIF display a FWHM of

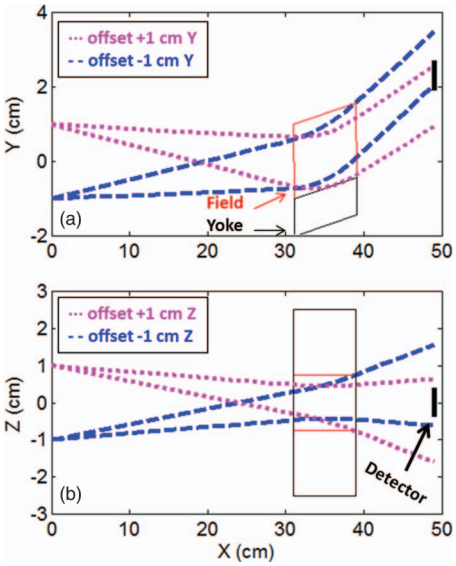

FIG. 5. Calculated 10 MeV proton trajectories for the MagPTOF system when the proton source location is offset by +1 cm (magenta dotted) and −1 cm (blue dashed) relative to the origin (a) in the bending plane (x,y) and (b) perpendicular to the bending plane (x,z). The protons were transported through the dipole magnetic field (black, red) to the detector (black). The MagPTOF system was found to be tolerant to offsets of this size, which translate to ±1.6° misalignment of the detector line-of-sight.

∼1 MeV. This spectral width corresponds to a time-of-flight broadening of approximately 500 ps, which dominates the observed temporal width of the proton signal and renders the temporal broadening due to the magnet negligible.

The advantages of a focusing magnet for increasing the proton signal were considered. However, such a magnet would have more stringent alignment requirements and would require better *a priori* knowledge of the incident proton spectrum. The expected proton signals with a non-focusing magnet are sufficient for making the desired measurement.

IV. SIGNALS AND BACKGROUND

The primary goal of this upgrade is to minimize background due to x-rays from the implosion while measuring the D^3He-proton signal. Based on D^3He-proton signals observed using the pTOF on NIF and OMEGA[8] and the effective solid angle of MagPTOF, the expected MagPTOF signal level for a typical shock D^3He-proton yield of 1×10^8 is approximately 50 mV. Because the x-ray background sources and the proton signal are separated by approximately 10 ns due to time-of-flight, which is several times the impulse response falloff time (∼1.4 ns), the detector has time to recover from x-rays prior to observing the protons. However, for a robust proton measurement, the peak x-ray background should be comparable to or smaller than the signals of interest. Possible background sources with the MagPTOF conceptual design have been thoroughly reviewed, including direct x-ray signal from the hohlraum, x-ray fluorescence in the magnet, shielding, and mounting hardware, and photo- and Compton-scattered electrons from the tungsten shielding.

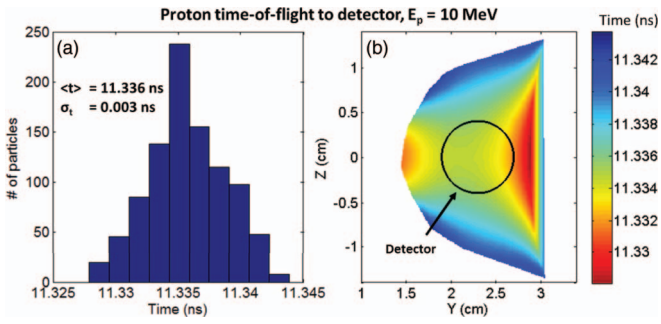

FIG. 6. (a). Calculated time-of-flight distribution for 10 MeV protons transiting the modeled magnetic field to the detector. The temporal broadening caused by the magnet is negligible ($\sigma = 3$ ps for 10 MeV protons, <7 ps for 6 to 16 MeV protons). (b) Time-of-Flight map for the 10 MeV protons at the detector plane. Particles within the black circle are detected.

X-ray-induced fluorescence in the magnet was found to be the most significant source of background. Although the magnet is composed primarily of iron, the primary source of fluorescent background is expected to be the neodymium due to the higher-energy x-rays produced ($E_{line} = 43.6$ keV, compared to 7.1 keV for iron) and the comparatively large probability of fluorescence ($P_{fluor} = 92.2\%$, compared to ∼34%).[11] Photons with 43.6 keV have a mean free path in the magnet material of $\lambda = 270$ μm, defining the volume of magnet material that can produce fluorescent background for the detector.

The number of photons incident on the magnet with energy high enough to stimulate fluorescence depends on the x-ray spectrum observed, as

$$N = \int_{E_{line}}^{\infty} \frac{S(E)}{E} \exp[-(\mu/\rho)_{\mathrm{Nd}} w_{\mathrm{Nd}} \rho_{mag} x_1] \Omega_1 dE, \qquad (1)$$

where S(E) is the spectrum of x-rays produced in the experiment, in units of keV/(keV Sr); $(\mu/\rho)_{\mathrm{Nd}}$ is the x-ray mass attenuation coefficient of neodymium[12] and $w_{\mathrm{Nd}} = 0.267$ is the mass fraction of neodymium in the magnet; ρ_{mag} is the density of the magnet; x_1 is the depth in the magnet from which fluorescent photons can escape; and Ω_1 is the solid angle of the inside magnet surface in Sr. If we assume that fluorescent photons from a depth of λ are able to escape and strike the detector, then from the geometry discussed in Sec. II, $x_1 \approx 2.6\lambda = 566.8$ μm.

The energy absorbed in the detector via neodymium K-shell fluorescence in the magnet is estimated conservatively as: $E_{abs} = NP_{fluor}E_{line}(\Omega_2/4\pi)P_{abs}f_{abs}$, where P_{abs} is the probability of photon absorption by the detector; Ω_2 is the solid angle of the magnet inner surface relative to the detector; and f_{abs} is the fraction of the photon energy absorbed in the detector. For Nd-fluorescence photons, the dominant absorption process in the detector is incoherent Compton scattering, but the average fraction of energy deposited by this process is only $f_{abs} = E_{line}/(M_e + E_{line}) \approx 8\%$. Because of this, the energy absorbed through Compton scattering and Photoelectric absorption are comparable, and the product $P_{abs}f_{abs} \approx 0.2\%$.

Numerically integrating over the measured spectrum S(E) from a typical shot with a peak laser power of 420 TW,[13] and scaling this model to the x-ray peaks observed by the existing pTOF, a background peak amplitude of 110 mV is expected, comparable to the expected proton signal. If necessary, this background may be further reduced by including

TABLE I. Summary of estimated background levels for MagPTOF.

Source of background	Estimated background
Nd K-shell fluorescence	110 mV (no filters at detector)
	7 mV (w/ filters at detector)
X-ray scatter from mounting bracket	14 mV
Direct x-rays	5 mV
e- scattered from W	<1 mV
Total	130 mV (no filters at detector)
	27 mV (w/ filters at detector)

additional filtering at the detector: the current standard proton filtering of 50 μm Ta + 100 μm Au would reduce fluorescent x-rays striking the detector by a factor of 15.

Other sources of background were also evaluated. The direct x-ray spectrum is dramatically reduced by the tungsten shield and produces only 5 mV of background. X-ray scattering from the detector mounting bracket, which has been found to be the primary source of background for the existing pTOF diagnostic when fielded with 2 cm tungsten shielding (~300 mV), is expected to produce 14 mV for MagPTOF as much less of the detector mounting bracket is directly exposed to TCC. Photo- and Compton-scattered electrons from the rear surface of the tungsten shielding are expected to produce a background of less than 1 mV. Other sources of background, such as x-ray fluorescence in the neighboring DIM hardware and neutron-induced fluorescence, have not been reviewed in detail, but simple estimates indicate they are negligible compared to the neutron and proton signals and the effects considered here. Complete modeling of the DIM hardware using GEANT4, a multi-physics Monte Carlo particle transport code, will be used to validate these estimates in the future. A summary of estimated contributions to the MagPTOF background may be found in Table I. These estimates are comparable to or less than the expected proton signals, allowing a robust measurement of D^3He-proton bang-time.

While the pTOF diagnostic has routinely measured compression-bang time using 2.45 MeV DD-neutrons, the additional mass of the magnet and shielding will scatter neutrons and change the detector's effective sensitivity and impulse response. The tungsten x-ray shielding has a single-scattering depth of approximately 2.5 cm for the DD-neutrons. For the default 2 cm shielding, it is estimated that the fraction of unscattered neutrons reaching the detector will be ~46% of the initial neutron fluence. Nearly all (>99%) of the neutrons scattered in the tungsten shielding will be deflected sufficiently to miss the detector. The detector occupies a solid angle fraction of approximately 0.0002 with respect to the shielding, while the neutrons are scattered over a fraction of approximately 0.1, with an average scattering angle of ~30°. For this reason, the neutrons scattered in the shielding are effectively lost to the measurement.

The substantial mass in the MagPTOF housing and magnet will also scatter DD-neutrons into the detector. These scattered neutrons will have longer path-lengths and reduced energy relative to the direct unscattered neutrons, resulting in a delayed arrival time at the detector. To evaluate the impact of such scattering on the observed neutron signal, a model of

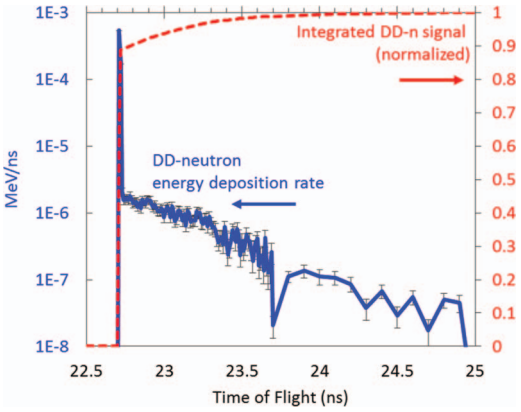

FIG. 7. Simulated energy deposition rate by DD-neutrons in the MagPTOF detector versus time (blue points). The Monte Carlo N-Particle Transport code MCNP5 was used for this calculation. The integrated neutron signal (red dashed line) reaches 89% of the total neutron signal within 20 ps of the expected arrival time for 2.45 MeV DD-neutrons, confirming that the scattered neutrons will not significantly perturb the DD-neutron measurement. The model incorporates the detector, 2 cm tungsten shielding, magnet, and MagPTOF housing in a simplified geometry.

neutron scattering in MagPTOF was developed using the particle Monte Carlo transport code MCNP5.[14] Neutron energy deposition in the detector was simulated as a function of time for a simplified version of the MagPTOF geometry including magnet, housing bracket, 2 cm tungsten shielding, and detector. In these simulations, 95% of the neutrons passing through the detector were unscattered. The scattered neutrons appear as a tail on the time-resolved neutron energy deposition in the detector, as shown in Figure 7. These scattered neutrons contribute only 11% of the total energy deposited by all neutrons. Due to the small amplitude of this signal tail, the analysis procedure for the DD-neutron signal peak as described in Ref. 8 will not be substantially impacted.

Based on these estimates of proton and neutron signals and x-ray background, a typical MagPTOF trace was simulated, as shown in Figure 8. This predicted signal is for a

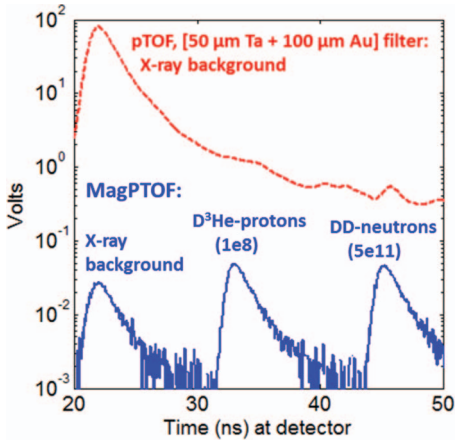

FIG. 8. Predicted signals and background for the MagPTOF system (blue) for a NIF implosion with an ion temperature of 3 keV demonstrate a clear record of both fusion species of interest, distinct from the x-ray background. This model includes standard additional filtering on the detector, focusing of the protons, and 54% neutron scattering in the tungsten shield, as well as a 1 mV noise floor associated with the recording system.[8] Compared to the existing pTOF diagnostic filtered to admit D^3He-protons (red dashed), the MagPTOF upgrade reduces the background by over three orders of magnitude.

TABLE II. Error budget for MagPTOF-measured compression-bang time (DD-n), shock-bang time (D^3He-p), and compression-shock bang time difference (ΔBT).

Source of uncertainty	Uncertainty
Crosstiming to laser system	±15 ps
Detector IRF (in situ)	±25 ps
Forward Fit (S/N = 10)	±18 ps
Cable repeatability shot-to-shot	±5 ps
Nominal detector distance	±0.5 mm →
DD-n, D^3He-p	±23 ps, 12 ps
On-shot alignment, typical	±1 mm →
DD-n, D^3He-p	±46 ps, 23 ps
Magnet temporal broadening	±7 ps (D^3He-p only)
Mean energy	±5 keV[a], 140 keV
DD-n, D^3He-p	→ ±23 ps, 79 ps
Total: DD-n, D^3He-p, ΔBT	±66 ps, 90 ps, 96 ps

[a]Fuel velocity ±20 km/s.

typical gas-filled hohlraum implosion with D^3He gas-filled target, producing a D^3He-proton yield of 1×10^8 and a DD-neutron yield of 5×10^{11}. Notably, the peak expected x-ray background has been reduced by over 3 orders of magnitude from the background in pTOF data when the diagnostic is filtered to admit D^3He protons. Such data would readily provide robust measurements of both the shock- and compression-bang times using the D^3He-proton and DD-neutron signals, respectively.

Since the detector, cables, signal recording system, and analysis procedure are all carried over from the pTOF diagnostic, the timing uncertainty budget for the MagPTOF upgrade, shown in Table II, is nearly identical to that reported in Ref. 8. The dominant uncertainty in the proton time-of-flight is the uncertainty in the proton energy, which is measured by the neighboring WRF with a typical uncertainty of ±140 keV.

V. CONCLUSIONS

The MagPTOF diagnostic has been designed for the NIF to simultaneously measure shock- and compression-bang time in D^3He gas-filled hohlraum implosions. This diagnostic, an upgrade of the existing pTOF diagnostic, incorporates a thick tungsten filter to shield the detector from high-energy x-rays generated by the hohlraum, and a magnet to deflect shock-generated D^3He-protons around the shielding and onto a CVD-diamond detector. Background from x-rays is estimated to be substantially smaller than the signals of interest. Neutron scattering in the shielding and magnet has been simulated and the results indicate that this background does not impact the ability to measure compression-bang time using DD-neutrons. This diagnostic capability will provide the first measurements of shock- and compression-bang time in surrogate D^3He gas-filled implosions at the NIF, which will mutually reinforce the proton spectral measurements of the ρR at shock-burn, providing a significant new constraint on modeling of the implosion dynamics.

ACKNOWLEDGMENTS

The authors thank the engineering and operations staff at NIF, LLE, and MIT for their support. This work was performed under the auspices of the U.S. Department of Energy by Lawrence Livermore National Laboratory under Contract No. DE-AC52-07NA27344. This work was done in part for H. Rinderknecht's Ph.D. thesis and was supported in part by the U.S. DoE (DE-FG52-09NA29553), LLNL (B580243), LLE (414090-G), the Fusion Science Center at the University of Rochester (415023-G), and the National Laser Users Facility (DE-NA0000877).

[1]E. I. Moses, Fusion Sci. Technol. **44**, 11 (2003), available online at: http://www.ans.org/pubs/journals/fst/a_304.
[2]J. Lindl, O. Landen, J. Edwards, E. Moses, and N. Team, Phys. Plasmas **21**, 020501 (2014).
[3]A. B. Zylstra *et al.*, "The effect of shock dynamics on compressibility of ignition-scale NIF implosions," Phys. Plasmas (unpublished).
[4]F. H. Séguin *et al.*, Rev. Sci. Instrum. **74**, 975 (2003).
[5]A. B. Zylstra *et al.*, Rev. Sci. Instrum. **83**, 10D901 (2012).
[6]D. G. Hicks *et al.*, Phys. Plasmas **19**, 122702 (2012).
[7]J. R. Rygg *et al.*, Phys. Rev. Lett. **112**, 195001 (2014).
[8]H. G. Rinderknecht *et al.*, Rev. Sci. Instrum. **83**, 10D902 (2012).
[9]N. Sinenian *et al.*, Rev. Sci. Instrum. **82**, 103303 (2011).
[10]W. J. Hibbard, M. D. Landon, M. D. Vergino, F. D. Lee, and J. A. Chael, Rev. Sci. Instrum. **72**, 530 (2001).
[11]M. Chadwick, M. Herman, P. Obložinský *et al.*, Nucl. Data Sheets **112**, 2887 (2011) [Special Issue on ENDF/B-VII.1 Library].
[12]J. H. Hubbell and S. M. Seltzer, (2004), Tables of X-Ray Mass Attenuation Coefficients and Mass Energy-Absorption Coefficients (version 1.4), available online at: http://physics.nist.gov/xaamdi [2013, July 1]. National Institute of Standards and Technology, Gaithersburg, MD.
[13]J. W. McDonald, R. L. Kauffman, J. R. Celeste, M. A. Rhodes, F. D. Lee, L. J. Suter, A. P. Lee, J. M. Foster, and G. Slark, Rev. Sci. Instrum. **75**, 3753 (2004).
[14]X-5 Monte Carlo Team, MCNP - A General Monte Carlo N-Particle Transport Code, Version 5, Report No. LA-UR-03-1987, Los Alamos National Laboratory, 2005.